https://doi.org/10.5194/acp-2020-955
Preprint. Discussion started: 12 October 2020

Atmospheric Chemistry and Physics
Discussions

Automated time-height-resolved airmass source attribution for profiling remote sensing applications

Martin Radenz[1], Patric Seifert[1], Holger Baars[1], Athena Augusta Floutsi[1], Zhenping Yin[1,2,3], and Johannes Bühl[1]

[1]Leibniz Institute for Tropospheric Research (TROPOS), Leipzig, Germany
[2]School of Electronic Information, Wuhan University, Wuhan, China
[3]Key Laboratory of Geospace Environment and Geodesy, Ministry of Education, Wuhan, China

Correspondence: Martin Radenz (radenz@tropos.de)

Abstract. Height resolved airmass source attribution is crucial for the evaluation of profiling ground-based remote sensing observations. This work presents an approach how backward trajectories or particle positions from a dispersion model can be combined with geographical information (a land cover classification and manually defined areas) to obtain a continuous and vertically resolved estimate of airmass source above a certain location. Ideally, such an estimate depends on as few as possible a-priori information and auxiliary data. An automated framework for the computation of such an airmass source is presented and two exemplary applications are described. Firstly, the airmass source information is used for the interpretation of airmass sources for three case studies with lidar observations from Limassol (Cyprus), Punta Arenas (Chile) and ship-borne off Cabo Verde. Secondly, airmass source statistics are calculated for two 8-week campaigns to assess potential observation biases of lidar-based aerosol statistics.

1 Introduction

Tracing airmass transport trough a turbulent atmosphere is (still) a complex and entangled problem. Especially the transport of aerosols and consequently the interaction with clouds, precipitation and radiation require to capture the four-dimensional history of an air parcel. When it comes to practical application, such as the analysis of aerosol observations or aerosol-cloud interaction studies, the ease of interpretation is often hindered by the amount of data that needs to be considered.

Models that simulate airmass transport can be broadly grouped into trajectory models and particle dispersion models (overview provided by Fleming et al., 2012). Trajectory models calculate the transport of a single air parcel imposed by the mean meteorological fields. The model simulations can be either run forward or backward in time, providing information about either the source or the destination of the airmass, respectively, after a given transport time. Turbulence and vertical motion during the transport process are usually parametrized on the grid scale. Commonly used models are HYSPLIT (Stein et al., 2015), FLEXTRA (Stohl et al., 1995) and LAGRANTO (Wernli and Davies, 1997; Tarasova et al., 2009). Due to the

https://doi.org/10.5194/acp-2020-955
Preprint. Discussion started: 12 October 2020

Atmospheric Chemistry and Physics Discussions

rather simple approach, the results are quite uncertain (Seibert, 1993; Polissar et al., 1999), but computational requirements are comparably low. A straightforward approach to represent some of the variability is to calculate spatial or temporal ensembles of the trajectories (Merrill et al., 1985; Kahl, 1993; Draxler, 2003). Lagrangian particle dispersion models (LPDM) with a large number of particles are set up to cover turbulent and diffusive transport even more realistically (Stohl et al., 2002). The fate of each particle is tracked individually, allowing more variability to be included into the transport simulation. A frequently used LPDM is FLEXPART (Pisso et al., 2019).

Generally, representation of chaotic motion in the atmosphere improves with larger ensembles of trajectories or increasing number of particles. But, with dozens to hundreds airmass locations available interpretation rapidly becomes cumbersome. Residence times are a well established technique for attributing regional information to airmass properties such as being laden with aerosols, moisture or trace gases (Ashbaugh, 1983; Ashbaugh et al., 1985). Using backward transport simulations, analysis of the residence time yields useful information about the potential source region of an observed airmass. The basic assumption is, that the longer an air parcel was present in a certain region, the more likely it will be influenced by the surface characteristics. Hence, the dimensionality of an air parcels 4D location can be reduced to the residence time. Approaches for clustering backward trajectories by direction, source regions or latitude is widely done. Most available approaches focus on the interpretation of timeseries observations at single heights - mostly close to ground (e.g. Escudero et al., 2011), for aircraft intersects (e.g. Paris et al., 2010) or over a whole region (Lu et al., 2012). More sophisticated approaches blend the residence time with actual concentration measurements (Stohl, 1996; Heintzenberg et al., 2013). However, these approaches require continuous concentration time series, which are generally not available for remote sensing observations. Furthermore any profile information above the measurement site is neglected.

When interpreting ground-based remote sensing observations the airmass sources are attributed by manually selecting periods (time and height above ground), that seem interesting for further investigation and calculating backward transport for that specific cases. For example optical properties of aerosol layers retrieved from lidar observations are frequently connected to airmass sources (e.g., Müller et al., 2007; Mattis et al., 2008). If airmass source estimates are required for longer time periods or multiple heights, calculating, visualizing and interpreting the results becomes tedious. Hence, a continuous, computationally efficient, easy to interpret and automated airmass source estimate is required. To be broadly and easily applicable, such a source estimate should not require extensive a-priori information, such as clusters of trajectories or potential source contribution functions. The required approach is intended to be also simpler than using a coupled aerosol model, such as CAMS (Flemming et al., 2017), COSMO-MUSCAT (Dipu et al., 2017) or ICON-ART (Rieger et al., 2015). Though these models can provide profiles of atmospheric composition, they usually do not provide information on the source.

In here, we propose a combination of automated backward trajectory calculations and geographical information for the setup of a simple, spatio-temporally resolved airmass source attribution scheme. As a proxy for geographical information, two products are used: a land cover classification mask and manually defined geographical areas. The methodology is described in the following section 2. An comprehensive, easy to use software package is also provided. Earlier versions were already used in Haarig et al. (2017), Foth et al. (2019) and Floutsi et al. (2020). Afterwards two applications illustrate potential use cases. In the first example, the temporal and vertical evolution of the airmass source is analyzed for three lidar observations of different

https://doi.org/10.5194/acp-2020-955
Preprint. Discussion started: 12 October 2020

aerosol conditions from Limassol (Cyprus), Punta Arenas (Chile) and on board R/V Polarstern off Cabo Verde. In the second application example, vertically resolved airmass source statistics are used to assess potential observation biases of long-term lidar-based aerosol statistics. Two 7-week campaigns out of the PollyNET dataset (Baars et al., 2016) are presented: Finokalia (Greece) and Krauthausen (Germany).

2 Airmass source attribution method

In a conceptualized view, properties of an air parcel arriving over a location of interest are characterized by a certain surface type, if the air was close to the surface during its past. The 'proximity' to the surface can be parameterized as a reception height, which depends on the mixing state of the atmosphere at this location as well as on the type of aerosol particles that could be potentially emitted (i.e. mineral dust or sea salt). Conceivable choices for the reception height are the model-derived depth of the atmospheric boundary layer or fixed thresholds. As a first estimate for identification of possible surface effects on an air parcel, $2\,\mathrm{km}$ is widely used (Val Martin et al., 2018). It is assumed that, the more time an air parcel resides close to the surface, the more likely it acquires the aerosol footprint of the surface. The residence time - the total time an air parcel spend over a certain surface below the reception height - is a first hint for the aerosol characteristics of the air parcel.

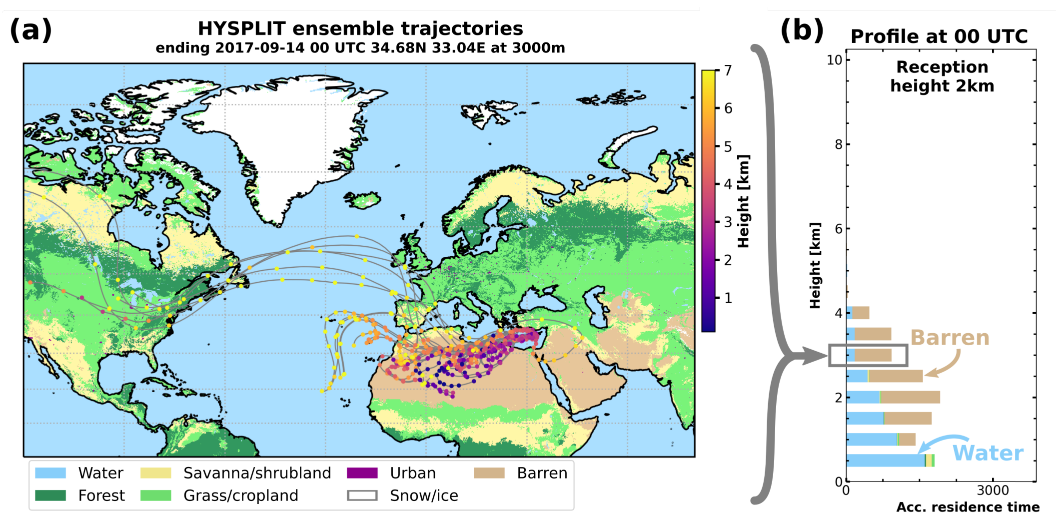

Figure 1. Example how the ensemble backward trajectories ending at Limassol on the 14 September 2017 at $3\,\mathrm{km}$ height (a) are used to calculate the profile of residence times per land surface class (b).

The transport pathway of an airmass arriving over the site can be computed either using mean wind trajectories or a particle dispersion model. Both approaches can be used with the proposed method. Mean wind trajectories for the past 10 days are calculated using HYSPLIT (Stein et al., 2015). To account for variability, ensemble trajectories consisting of 27 members, spaced $0.3°$ horizontally and $220\,\mathrm{m}$ vertically around the end point, are used (Fig. 1 a). Meteorological input data for HYSPLIT are taken from the GDAS1 dataset ($1°$ horizontal resolution) provided by the Air Resources Laboratory (ARL) of the U.S.

https://doi.org/10.5194/acp-2020-955
Preprint. Discussion started: 12 October 2020

Atmospheric Chemistry and Physics
Discussions

MODIS Category	Simplified Category
0	water
1, 2, 3, 4, 5, 6	forest
7, 8, 9	savanna/shrubland
10, 11, 12, 14	grass-, cropland
13	urban
15	snow
16	barren

Table 1. Overview, how the MODIS land surface categories translate into the simplified categories used in this study. MODIS Category numbers as in (Broxton et al., 2014)

National Weather Service's National Centers for Environmental Prediction (ARL Archive). The location of the air parcel is stored in steps of 1 hour. A more realistic representation of turbulence and mixing can be achieved using a LPDM, which simulates the pathway of hundreds to thousands of particles. Here the recent version of FLEXPART (Stohl et al., 2005; Pisso et al., 2019) is used. Meteorological data is obtained from the GFS analysis at a horizontal resolution of 1° (NOAA, 2000). 5000 particles are used with the particle positions being stored every 3 hours. These simulations are run every 3 hours with height steps of 500 m for the whole period of interest.

In this work, surface is classified by two methods: (1) a simplified version of the MODIS land cover classification (Friedl et al., 2002; Broxton et al., 2014). The 17 categories of the original dataset are grouped to 7 categories according to Tab. 1 in order to allow for purpose-serving statistics in the output. Additionally, the horizontal resolution is reduced to 0.1°. The categories do not resolve the annual cycles, for example due to growing seasons. (2) customly defined areas as polygons, named according to their geographical context.

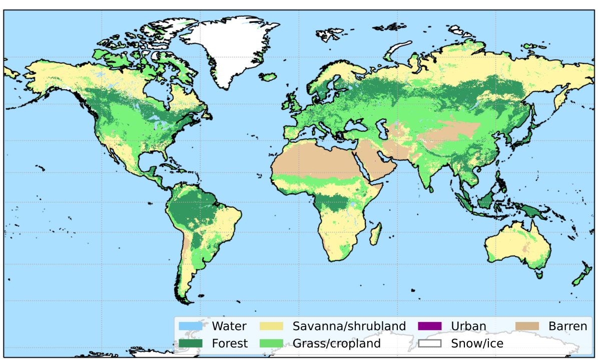

Figure 2. The simplified MODIS land cover classification. Details are given in the text.

https://doi.org/10.5194/acp-2020-955
Preprint. Discussion started: 12 October 2020

Atmospheric Chemistry and Physics
Open Access
EGU
Discussions

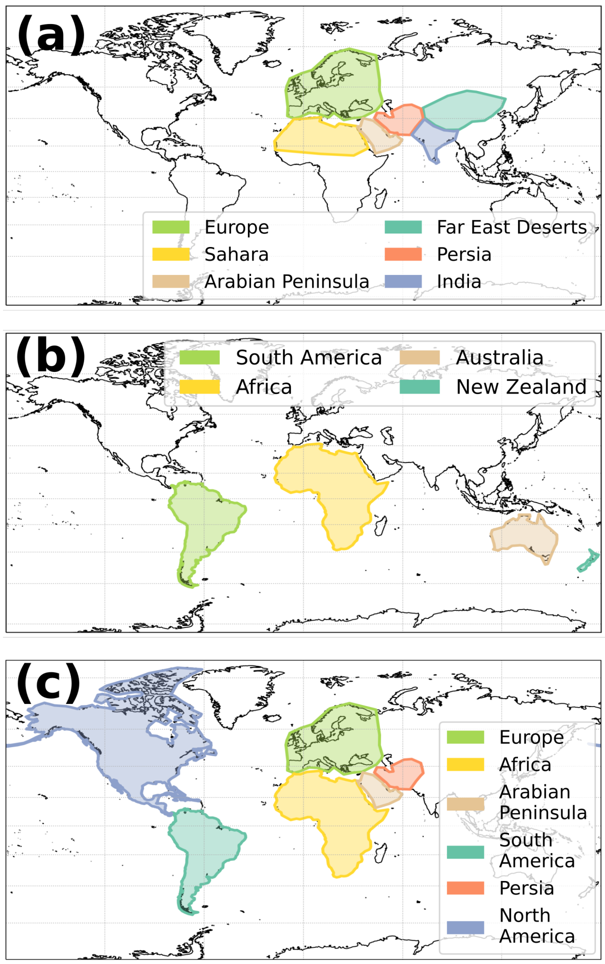

Figure 3. The customly defined geographical areas for Limassol (a) and Punta Arenas (b) and the Atlantic transit (c).

The residence times at each time and height step are summed for each land cover class or polygon, where the backtrajectory or particle was below the reception height. Within this study the widely applicable reception height threshold of $2\,\mathrm{km}$ is used (Val Martin et al., 2018). Different settings can be easily applied to study events which are entrained at greater heights, such as wildfire smoke emission or volcanic eruptions. The vertical airmass transport during such events is usually not accurately covered by atmospheric models. Setting the reception height to the maximum emission height of such events (as can be estimated, e.g., from satellite observations) can bypass the uncertainties in the modeled vertical motion. The residence times for each category and each height can then be visualized as a profile (Fig. 1 b). Where the residence time is 0, no air parcels were observed below the reception height during the duration of the backward simulation. In the example shown in Fig. 1 (b) above $5\,\mathrm{km}$ height, no airmasses resided at heights below $2\,\mathrm{km}$ above ground in the prior 10 days. The theoretical maximum residence time in hours depends on the number of trajectories or particles n, the duration of backward calculation d in days

https://doi.org/10.5194/acp-2020-955
Preprint. Discussion started: 12 October 2020

Atmospheric Chemistry and Physics
Discussions

and the interval of output Δo in hours:

$$t_{\max} = n\,d\,\frac{24}{\Delta o} \tag{1}$$

To illustrate the temporal evolution, successive airmass source profiles can be shown one after each other. This visualization condenses the 4D history of a multitude of trajectories (or thousands of particle positions) to a quickly understandable summary, which closely resembles the time-height cross section as usually obtained from vertically or nadir pointed active ground-based remote sensing observations (e.g., Fig. 4).

3 Polly$^{\mathrm{XT}}$ lidar observations

The airmass source estimate is used to interpret observations conducted with the Polly$^{\mathrm{XT}}$ lidar (Engelmann et al., 2016). Polly$^{\mathrm{XT}}$ is equipped with backscatter-channels at 1064, 532 and $355\,\mathrm{nm}$ as well Raman- and depolarization-channels at the shorter two wavelengths. The optical properties are derived using the automated PollyNET retrieval (Baars et al., 2016, 2017; Yin and Baars, 2020) and manual analysis of single profiles. One product of this retrieval is the quasi backscatter coefficient, where the attenuated backscatter is corrected for molecular extinction. Details are covered in Baars et al. (2017).

Polly$^{\mathrm{XT}}$ was deployed to various field campaigns and longer term measurements during the last 15 years (Baars et al., 2016). A broad variety of meteorological conditions and aerosol regimes was covered. The multi-wavelength observations of Polly$^{\mathrm{XT}}$ contain unique fingerprints of the observed aerosol types from different source regions (Illingworth et al., 2015).

In the following sections 4 and 5, the airmass source attribution will be applied to selected case studies and measurement campaigns, in order to demonstrate its applicability for determination of the airmass source regions and for the estimate of potential observation biases. The case studies are taken from deployments of Polly$^{\mathrm{XT}}$ to Limassol (Cyprus, 34.7°N, 33.0°E, 12m a.s.l., October 2016 to March 2018), Punta Arenas (Chile, 53.1°S, 70.9°W, 10m a.s.l., November 2018 and ongoing) and the RV *Polarstern* Atlantic transit 2018 when passing Cabo Verde (18.1°N, 21.3°W to 21.3°N, 20.8°W). The estimate of potential observation biases is done for the campaigns at Krauthausen (Germany, 50.9°N, 6.4°E, 99m a.s.l., April/May 2013) and Finokalia (Greece, 35.3°N 25.7°E, 250m a.s.l., June/July 2014).

4 Application to lidar case studies

4.1 Saharan dust off the coast of West Africa

A lofted layer of dust was observed on 30 and 31 May 2018 by a Polly$^{\mathrm{XT}}$ system on board RV *Polarstern* (Strass, 2018), as the ship steamed between Cabo Verde and African mainland (18.1°N, 21.3°W to 21.3°N, 20.8°W) on her transit north from Punta Arenas (Chile) to Bremerhaven (Germany). A detailed description of the event and optical properties of the observed aerosol were already reported by Yin et al. (2019).

Fig. 4 illustrates the temporal evolution of the observed aerosol plume by means of the time-height cross section of the $1064\,\mathrm{nm}$ quasi backscatter coefficient for the time period from 30 May 06 UTC to 31 May 06 UTC. Yin et al. (2019) discussed

https://doi.org/10.5194/acp-2020-955
Preprint. Discussion started: 12 October 2020

in detail the time and height period of the observation which is marked by a horizontal orange bar in Fig. 4 (their Fig. 14). According to the optical properties they argued that the lowest $1\,\mathrm{km}$ was dominated by marine particles and a certain contribution from European continental aerosol. At larger heights, a Saharan dust plume was present. Yin et al. (2019) corroborate their findings by ensemble calculations of HYSPLIT backward trajectories for selected arrival heights and times. However, this way of presentation is rather selective, as information for different heights and times can hardly be shown. This is where the benefit of the continuous airmass source estimate becomes evident. Fig. 5 presents the results of the airmass source estimate for the land surface classification and geographical areas for both, the HYSPLIT (Fig. 5 a,c) and the FLEXPART simulations (Fig. 5, b,d). The estimates based on HYSPLIT and FLEXPART show a good general agreement. The heights and times of certain surface types and geographical regions agree qualitatively. Before 12 UTC on 30 May 2018, FLEXPART derived a lower residence time from barren and grassland or 'Africa', respectively. With respect to Fig. 4, this seems to be reasonable as the layer was rather faint at the beginning of the shown measurement period. Besides this difference, both the HYSPLIT and FLEXPART approaches provide a concise picture of the likely source regions of the observed aerosol. Below $1.5\,\mathrm{km}$ height, the airmass was marine dominated with a small contribution of European grass/cropland. At heights between 2 and $4\,\mathrm{km}$, barren areas from Africa are the main source, but a considerable fraction is also attributed to African grass/cropland and Savanna. This finding is supporting the observations presented by Yin et al. (2019) who already discuss that there was likely a small non-dust fraction in the upper layer, as the particle depolarization ratio profile was not constant at all heights. A potential reason for the observed discrepancy of the observations from pure-dust conditions could be the presence of wildfire smoke stemming from the crop/grassland and savanna. In comparison to the lidar observations, the top of the layer was slightly underestimated by the airmass source estimate. The temporal extent is also fully captured. Variability of backscatter within the layer is not represented by the airmass source estimate, because the strength of dust mobilization is only insufficiently parametrized by the reception height. However, the airmass transport is correctly covered by both estimates. Interestingly, the airmass source estimation for this case provides some added value information with respect to the lidar observations. As both HYSPLIT and FLEXPART approaches indicate, North-American air masses were present in the upper troposphere during the time of the observation, which however had too low aerosol load for being detectable by the Polly$^{\mathrm{XT}}$ lidar.

4.2 Saharan and Arabian dust at Limassol, Cyprus

On the 14 September 2017 an upper-level short-wave trough moved eastward from the Aegean Sea towards Cyprus. Above $1\,\mathrm{km}$ height, the wind turned from South-West to South during the course of the day with velocities ranging from $5-15\,\mathrm{m\,s^{-1}}$, whereas below, wind velocity was lower and direction more variable.

The time-height cross-section of quasi backscatter observed by Polly$^{\mathrm{XT}}$ at Limassol shows two pronounced aerosol layers above the boundary layer (Fig. 6)). The first layer was observed between 1 and $2\,\mathrm{km}$ height from 0 to 9 UTC and a second, thicker layer after 3 UTC. Until the night, this layer increases in thickness from bases at 3 and tops at $4.5\,\mathrm{km}$ height to bases at 1.2 and tops at $6.5\,\mathrm{km}$ height. The boundary layer itself is also laden with aerosols and shows significant backscatter below $1\,\mathrm{km}$ height.

Atmospheric Chemistry and Physics Discussions

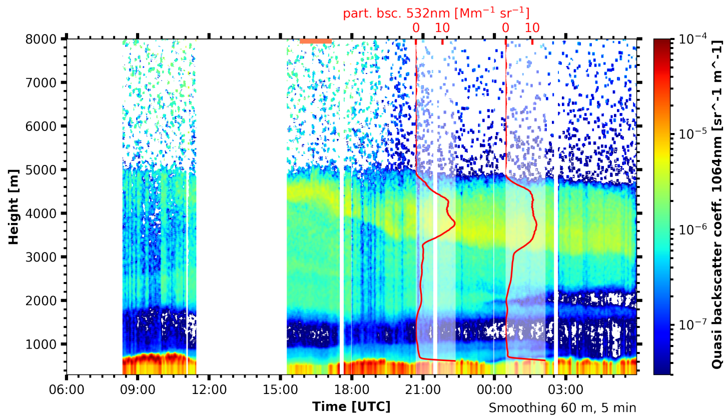

Figure 4. Quasi backscatter coefficient at $1064\,\mathrm{nm}$ observed by Polly$^{\mathrm{XT}}$ on board Polarstern on the 30 and 31 May 2018. Moving average smoothing of 8 range bins ($60\,\mathrm{m}$) and 10 temporal bins (5 minutes) was applied. The red overlays show the Klett derived particle backscatter coefficient from the automated algorithm at $532\,\mathrm{nm}$. The time period of manual analysis (see text) is marked by a horizontal orange bar.

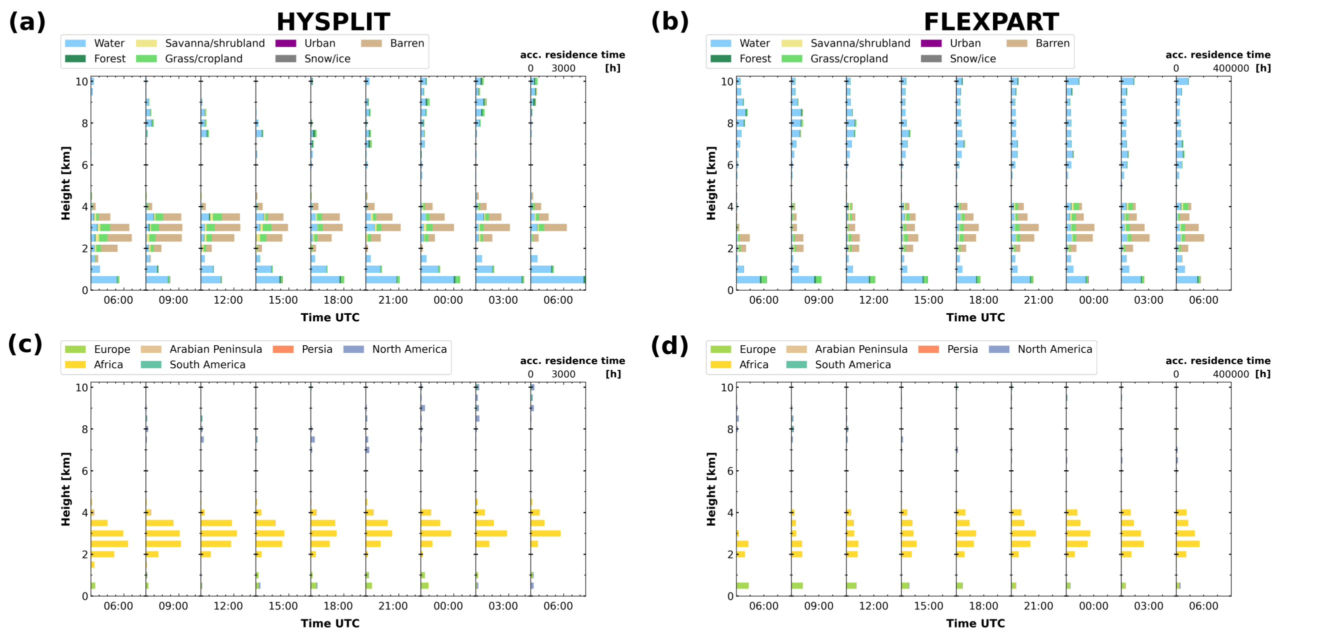

Figure 5. Airmass source estimate from 06 UTC on the 30 to 06 UTC on the 31 May 2018 for the land surface classification (a, b) and the named geographical areas (b, d) based on HYSPLIT (a, c) and FLEXPART (b, d).

The optical parameters were analyzed for one period in the morning between 02:59 and 04:02 UTC and one in the evening between 21:41 and 22:39 UTC (periods marked in Fig. 6 with horizontal orange bars). The profiles from the morning period (Fig. 7) show for the lower layer at $1.8\,\mathrm{km}$ height particle depolarization ratios of 0.25, low Ångström values and lidar ratios

https://doi.org/10.5194/acp-2020-955
Preprint. Discussion started: 12 October 2020

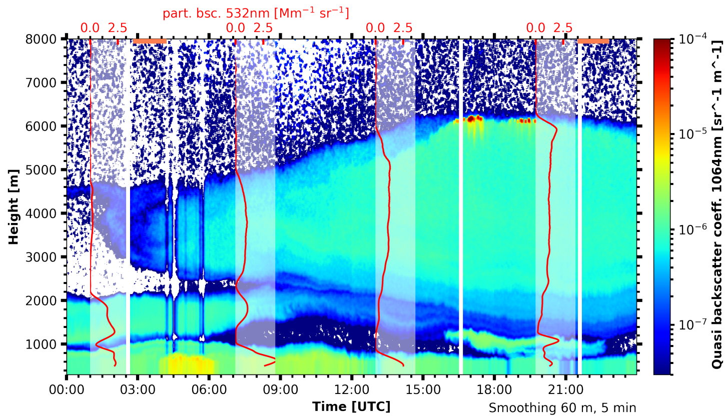

Figure 6. Quasi backscatter coefficient at $1064\,\mathrm{nm}$ observed by Polly$^{\mathrm{XT}}$ at Limassol on the 14 September 2017. Moving average smoothing of 8 range bins ($60\,\mathrm{m}$) and 10 temporal bins (5 minutes) was applied. The red overlays show the Klett derived particle backscatter coefficient at $532\,\mathrm{nm}$. The time periods of manual analysis (Fig. 7 and 8) are marked by horizontal orange bars.

of around $40\,\mathrm{sr}$. These optical parameters and their independence of wavelength are typical for aerosol mixtures with a high dust fraction. Extinction in this layer peaks at $72\,\mathrm{Mm}^{-1}$. The second layer above $2.5\,\mathrm{km}$ height has particle backscatter values of less than $2\,\mathrm{Mm}^{-1}\,\mathrm{sr}^{-1}$ (at $355\,\mathrm{nm}$) and $0.5\,\mathrm{Mm}^{-1}\,\mathrm{sr}^{-1}$ (at $532\,\mathrm{nm}$). Ångström values are slightly higher than in the lower layer, varying between 1 and 2. The particle depolarization ratios at both, 355 and $532\,\mathrm{nm}$ wavelength, are between 0.05 and 0.10.

During the evening (Fig. 8), the upper layer extended from 1.3 to $6\,\mathrm{km}$ height and shows homogeneous and mostly wavelength-independent optical properties throughout it's depth. Particle depolarization ratios were between 0.10 and 0.15, with $532\,\mathrm{nm}$ values slightly higher than at $355\,\mathrm{nm}$. Lidar ratios in that layer were $35\,\mathrm{sr}$, typical for middle east dust (Mamouri et al., 2013; Nisantzi et al., 2015) and a mixture of mineral dust and anthropogenic pollution (e.g. Tesche et al., 2009).

The airmass source estimate (Fig. 9) identifies transport from barren-ground-influenced air from the 'Sahara' until 9 UTC. Later, corresponding to the change in wind direction, the source for the air aloft is identified as 'Arabian Peninsula', but still the barren class. Below $1\,\mathrm{km}$ height, a mixture of surfaces was observed, originating mostly form 'Europe'. Comparing the source estimate based on HYSPLIT (Fig. 9 a, c) with the one from FLEXPART (Fig. 9 b, d), both models agree qualitatively well again. While the general transition was captured by the source estimate, the leading edge of the 'Arabian Peninsula' plume was observed over Limassol earlier than indicated. The increase in thickness of this plume is represented in the source estimate as well.

4.3 Biomass burning aerosol at Punta Arenas, Chile

Punta Arenas is located in a region where the atmosphere is known to be clean and one of the least affected by anthropogenic influences (Hamilton et al., 2014). Nevertheless, events of aerosol long-range transport also occur occasionally (Foth et al.,

https://doi.org/10.5194/acp-2020-955
Preprint. Discussion started: 12 October 2020

Atmospheric Chemistry and Physics Discussions

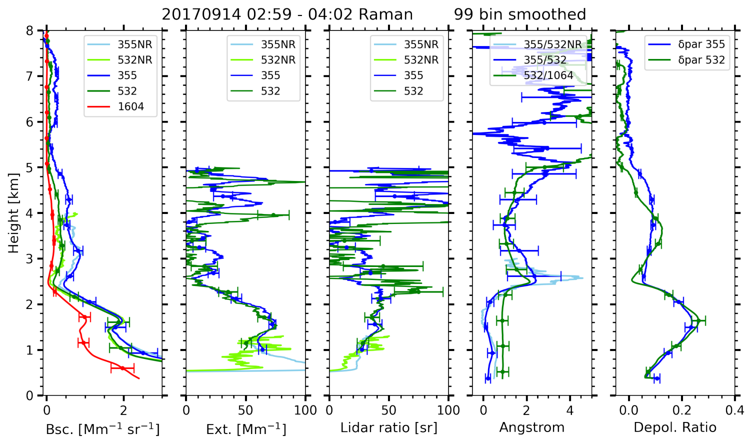

Figure 7. Profiles of optical properties on the 14 September 2017 between 02:59 and 04:02 UTC manually derived with the Raman method. A smoothing length of 99 bins (742.5 m) was applied.

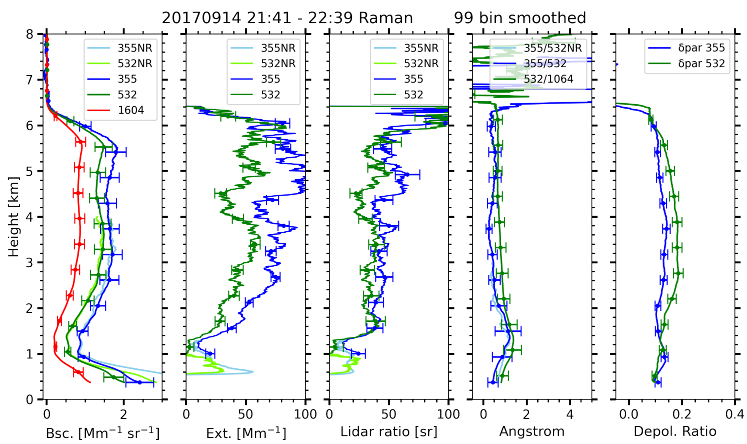

Figure 8. Profiles of optical properties on the 14 September 2017 between 21:41 and 22:39 UTC manually derived with the Raman method. A smoothing length of 99 bins (742.5 m) was applied.

2019; Floutsi et al., 2020). Due to the large distance of Punta Arenas from aerosol source regions, an attribution of observed aerosol events is in general rather complicated at this site. The application of airmass source estimate for the characterization of one aerosol long-range transport event is presented in here. An upper-level ridge was located off the Chilean coast on 20 May 2019, which supported also a surface high pressure system. At Punta Arenas the flow was zonal throughout the troposphere. Within that flow long-range transport from across the Pacific Ocean occurred.

In the Polly$^{\mathrm{XT}}$ observations from 20 May 2019 a layer of increased backscatter is present from 2 UTC to roughly 10 UTC. This layer extends from $3\,\mathrm{km}$ to above $6\,\mathrm{km}$ height (Fig. 10). The values of particle backscatter were peaking at $0.3\,\mathrm{Mm}^{-1}\,\mathrm{sr}^{-1}$

https://doi.org/10.5194/acp-2020-955
Preprint. Discussion started: 12 October 2020

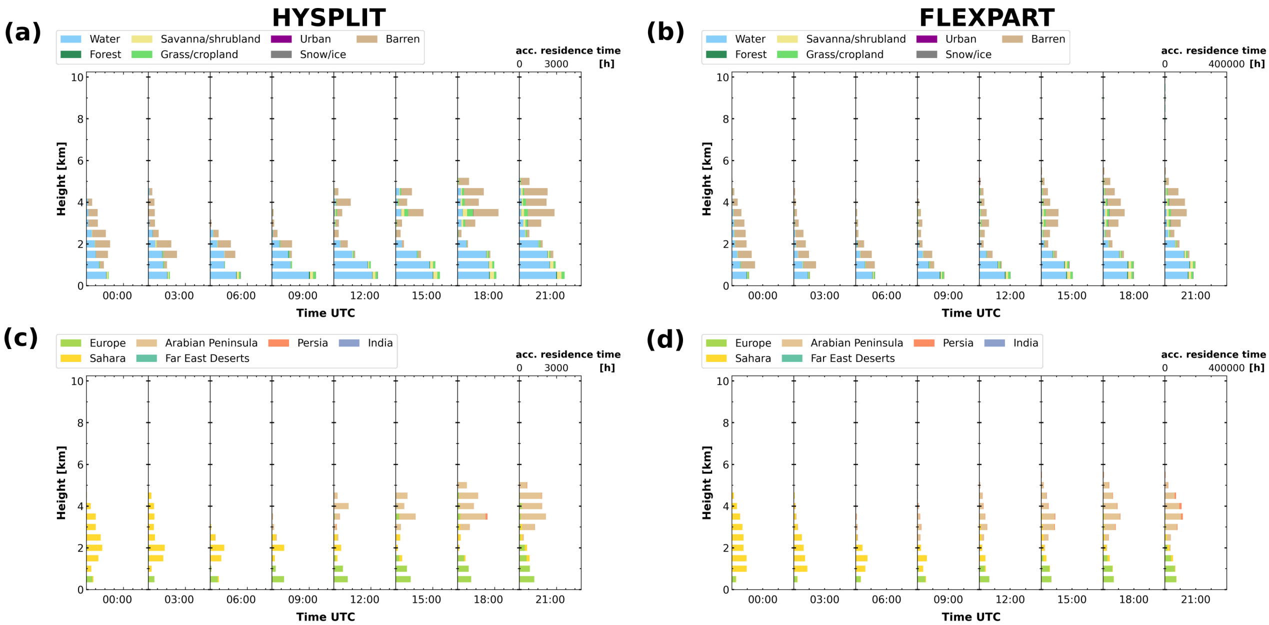

Figure 9. Airmass source estimate on the 14 September 2017 for the land surface classification (a, b) and the named geographical areas (b, d) based on HYSPLIT (a, c) and FLEXPART (b, d).

(Fig. 11), which are significantly lower values than reported for the prior cases. In the period analyzed, extinction values were approximately $15\,\mathrm{Mm}^{-1}$ giving lidar ratios well above $50\,\mathrm{sr}$ and rather low linear particle depolarization ratios. Altogether these optical parameters agree with prior findings of wildfire smoke in the troposphere (Tesche et al., 2011; Burton et al., 2012; Groß et al., 2013; Veselovskii et al., 2015).

The airmass soruce estimate is also able to capture this faint aerosol layer. Fig. 12 shows, that airmasses form 'Australia' were present between 3 and 9 UTC from 3 to $6\,\mathrm{km}$ height. In terms of land cover class these airmasses were characterized by savanna/shrubland and grass. Apart from the described period, the airmasses were solely influenced by the Southern Ocean (i.e. the water class). FLEXPART simulations (Fig. 12 b, d) agree with the HYSPLIT results, however the computed temporal extend and the residence times are slightly longer for the latter. Hence, the airmass source scheme is also capable of capturing aerosol transport at hemispheric (i.e. more than $10000\,\mathrm{km}$) scales.

5 Assessing potential observation biases

Vertically resolved aerosol statistics are prone to observations biases, as they usually depend on cloud-free conditions. When clouds or precipitation are present, no aerosol properties can be obtained from optical techniques. However, respective statistics, for example, obtained from lidar observations provide key quantities for the determination of the environmental conditions at a certain site (Matthias et al., 2004; Winker et al., 2013; Baars et al., 2016). It is therefore an open question whether the data

https://doi.org/10.5194/acp-2020-955
Preprint. Discussion started: 12 October 2020

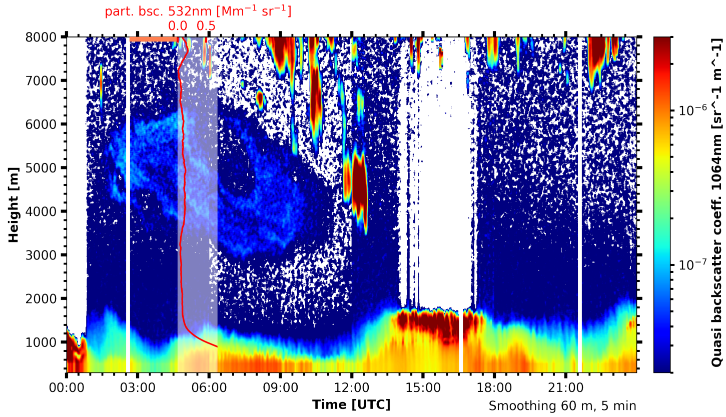

Figure 10. Quasi backscatter coefficient at $1064\,\mathrm{nm}$ observed by Polly$^{\mathrm{XT}}$ at Punta Arenas on the 20 May 2019. Moving average smoothing of 8 range bins ($60\,\mathrm{m}$) and 10 temporal bins (5 minutes) was applied. The red overlay shows the Klett derived particle backscatter coefficient at $532\,\mathrm{nm}$. The time period of manual analysis (Fig. 11) is marked by a horizontal orange bar.

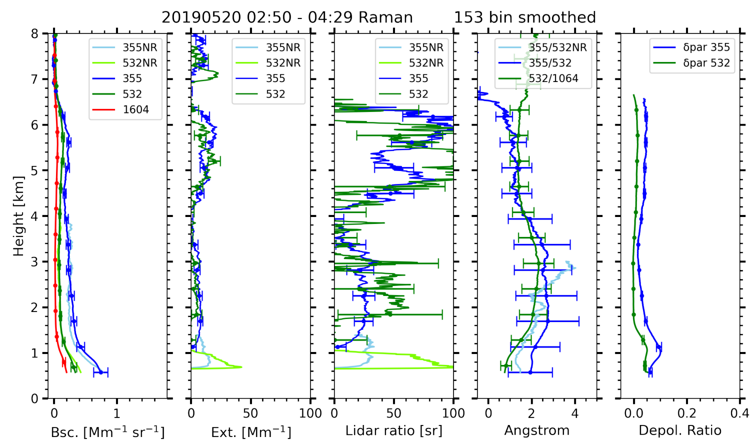

Figure 11. Profiles of optical properties on the 20 May 2019 between 02:50 and 04:30 UTC manually derived with the Raman method. A smoothing length of 153 bins ($1147.5\,\mathrm{m}$) was applied.

from suitable (cloud-free) measurement periods are representative for the full observational period. Chances are given that cloudy conditions are related to certain air masses which would stay unidentified in the lidar-based statistics of aerosol optical properties. One way to assess this bias is to compare the airmass residence time statistics of the full observational period with the one subsampled to the times when aerosol information is available.

Applied to lidar data, the automatically analyzed profiles of particle backscatter at $532\,\mathrm{nm}$ from Baars et al. (2016) are used. In their work, the raw profiles are grouped into 30-minute chunks, are cloud screened, averaged and analyzed by either the Klett or the Raman method, if signal-to-noise ratio is high enough and a reference height could be set. All profiles that pass a

https://doi.org/10.5194/acp-2020-955
Preprint. Discussion started: 12 October 2020

Atmospheric Chemistry and Physics Discussions

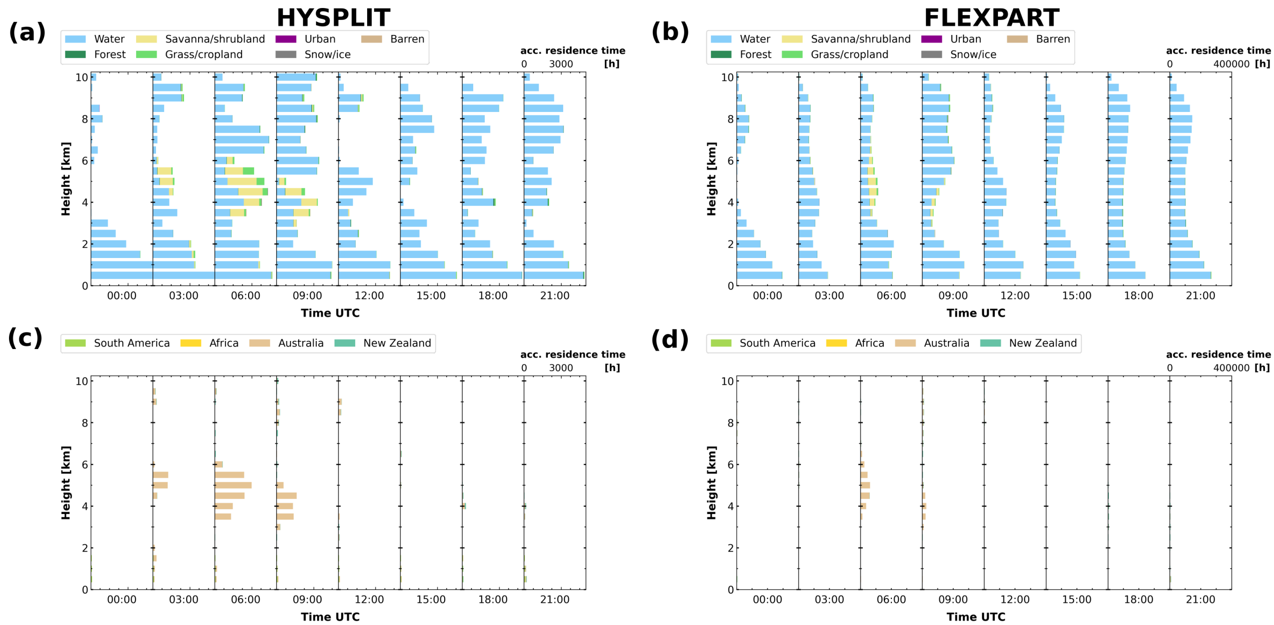

Figure 12. Airmass source estimate on the 20 May 2019 for the land surface classification (a, b) and the named geographical areas (b, d) based on HYSPLIT (a, c) and FLEXPART (b, d).

basic quality control are then included into the backscatter statistics. Obviously, this statistic will only be intermittent, due to overcast cloud conditions or interruptions in the measurement. Subsampling the airmass source statistics is done by selecting only the airmass source profiles that are temporally close to a valid lidar profile. A time-threshold of $1.5\,\mathrm{h}$ is used for the following statistics. However, covering representative airmass conditions is only a necessary condition, not a sufficient one to obtain a representative aerosol statistics.

Exemplary, the Polly$^{\mathrm{XT}}$ observations at Krauthausen (Germany, April/May 2013) and Finokalia (Greece, June/July 2014) are used here. At Finokalia 940 profiles could be analyzed with the Klett method. Hence, the particle backscatter statistics covers $457.7\,\mathrm{h}$, which is $38\,\%$ of the campaign duration. The statistics of particle backscatter is shown in Fig. 13 (a). For the Krauthausen deployment 315 profiles could be analyzed with the Klett method, covering $154.2\,\mathrm{h}$ or $11\,\%$ of the campaign. Fig. 14 (a) shows the particle backscatter statistics.

Profiles of airmass source for the Finokalia deployment are shown in Fig. 13 (b, c). Again with a reception height threshold of $2\,\mathrm{km}$. The summed residence time of subsampled profiles is divided by the fraction of time covered to make them comparable to the full residence time. Most dominant land surface categories are water, barren and grass-/cropland. The residence time of airmasses originating over barren ground shows a pronounced maximum between 2 and $6\,\mathrm{km}$ height. The residence time of all other categories decreases monotonically. Airmasses from urban and snow or ice covered areas are 10-100 times less frequent, than the other categories.

https://doi.org/10.5194/acp-2020-955
Preprint. Discussion started: 12 October 2020

Atmospheric Chemistry and Physics Discussions

In terms of geographical areas (Fig. 13 c), 'Europe' is the most dominant source up to 3 km and again above 9 km height. Between 3 and 6 km height the 'Sahara' is the most dominant airmass source. During the campaign period, no airmasses form the 'Arabian Peninsula', that fulfilled the $< 2\,\mathrm{km}$ criterion were transported to Finokalia.

The dominant sources are well covered by the lidar profiles in terms of land surface, only the barren class is subsampled by
230 a factor of 10 above 6.5 km height (Fig. 13 b). This agrees to the Sahara also being subsampled above that height. Airmasses originating over 'Europe' were also subsampled at heights above 5 km.

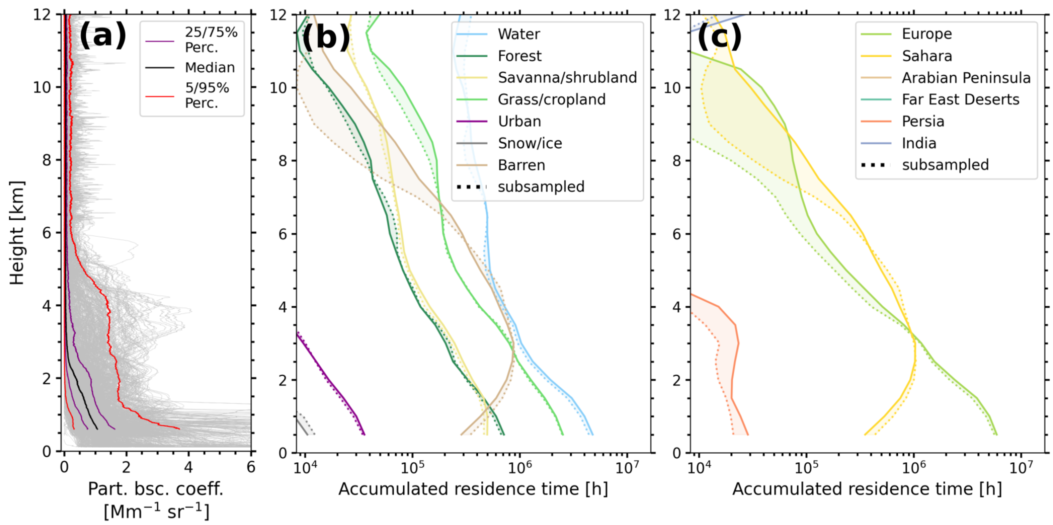

Figure 13. Statistics of particle backscatter coefficient (a, as in Baars et al., 2016) and airmass source estimate based on FLEXPART for the Finokalia campaign of Polly$^{\mathrm{XT}}$ in June and July 2014. The land surface classification (b) and the named geographical areas (c) are shown for the full duration (solid) and subsampled only for the periods with available lidar data (dotted). The subsampled residence times are divided by the fraction of time covered. The reception height threshold is 2 km.

During the Krauthausen campaign airmasses originating over water were the most frequent ones, followed by grass-/cropland, forest, shrubland and barren (Fig. 14 b). Again the residence times of the barren class show a distinct peak between 6 and 8 km height. Airmasses form the 'Sahara' area agree with the barren class (Fig. 14 c). As expected, 'Europe' is the dominant airmass
235 source in the lowest 6 km height, but due to increasing residence times with height for the 'Sahara' source, both are equally frequent in the upper troposphere. In the lidar observations, 'Europe' is potentially undersampled by 70 % between 1 and 10 km height, which is consistent with the grass/cropland and forest class also being undersampled. Barren land surfaces and 'Sahara' are oversampled by approximately 20 % up to 7 km height. In the lowermost 2 km height the land surface classes urban and snow/ice also contribute to the airmass mixture and are slightly oversampled.

https://doi.org/10.5194/acp-2020-955
Preprint. Discussion started: 12 October 2020

Atmospheric Chemistry and Physics Discussions

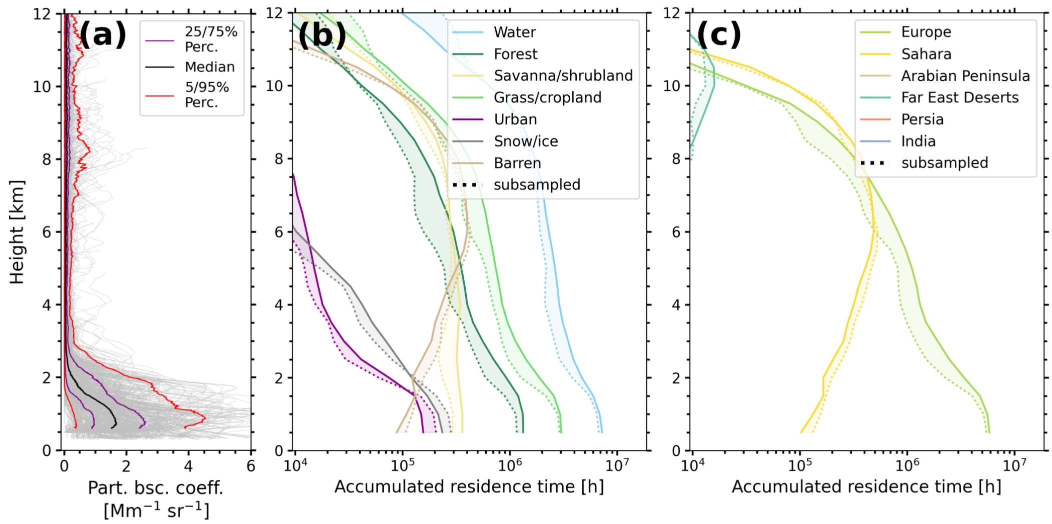

Figure 14. Statistics of particle backscatter coefficient (a, as in Baars et al., 2016) and airmass source estimate based on FLEXPART for the Krauthausen campaign of Polly^{XT} in April and May 2013. The land surface classification (b) and the named geographical areas (c) are shown for the full duration (solid) and subsampled only for the periods with available lidar data (dotted). The subsampled residence times are divided by the fraction of time covered. The reception height threshold is $2\,\mathrm{km}$.

6 Discussion and Conclusions

In this study we propose an easy to use method for a continuous, height-resolved automated airmass source estimate. By the combination of airmass transport modeling with geographical information, the dimensionality can be reduced and straightforward visualizations accelerate the interpretation of airmass origin. The airmass source estimate can be used to assist (profiling) aerosol observations, as aerosol load and characteristics are strongly controlled by surface properties and atmospheric transport. Three case studies illustrated the applicability at different sites and under different large scale flow conditions It was also shown how the source estimate supports the interpretation of lidar case studies and how potential observation biases can be investigated for longer term campaigns.

The major constrains of the proposed method are discussed in the following. While the airmass transport itself is generally covered well by trajectory models or LPDMs, the linkage to aerosol properties has to be done with care. Firstly, the reception height is modeled by using the mixing depth of the input fields or fixed values for all surfaces and aerosol particles, where differences could be expected for example for dust, smoke or wildfire smoke. Nevertheless for a first estimate, the assumption for a general reception height might be valid and can be improved in future. The $2\,\mathrm{km}$ height used in this work were also reported by other studies (e.g. for wildfires Val Martin et al., 2018) and seem to be applicable over wide ranges of climates and meteorological conditions. Summarizing, a high residence time over a certain class is only a necessary, not a sufficient condition for aerosol load of an air parcel.

https://doi.org/10.5194/acp-2020-955
Preprint. Discussion started: 12 October 2020

Atmospheric Chemistry and Physics
Open Access
EGU
Discussions

Secondly, aerosol particles might be removed by (wet) deposition between the source and observation site. Currently, such processes are not sufficiently reproduced in trajectory models or LPDMs, as they require detailed representation of aerosol microphysics and precipitation amount. Some improvements in this regard incorporated in the most recent version of FLEXPART (Pisso et al., 2019). However, deposition changes only the aerosol load of an air parcel, not the airmass source itself. Judging from the airmass source residence times alone, this process cannot be distinguished from cases where no emission happened in the first place. These questions could be addressed in future with a fully fledged aerosol transport model that also includes a tracer of airmass origin similar to the scheme shown here.

Some uncertainty is caused by the turbulent nature of the transport. For HYSPLIT a first estimate for the uncertainty of a single parcel location is 20 % of the distance from the trajectories origin (Stohl, 1998). Hence, for HYSPLIT a 27-member ensemble was used, to attribute for this uncertainty. Compared to HYSPLIT, the LPDM FLEXPART allows for a more realistic representation to turbulent transport, as well as a better sampling, when using hundreds or thousands of particles. However, a qualitatively good agreement between the both simulations suggests, that the presented airmass source estimate is rather robust considering uncertainty in the models.

In summary, the described compromises are necessary to get a continuous, height-resolved automated and airmass source estimate. The proved source code allows to use FLEXPART particle positions and HYSPLIT trajectories as an input. User-defined named geographical areas can be easily added. The runtime enviroment is provided as a docker container, including FLEXPART v10.4. With that setup one day of airmass source estimate with the resolution used in this study can be processed in less than an hour on a standard desktop computer (2.1 GHz processor, 4 GB RAM, single-threaded) .

Apart from the shown applications, this approached can be utilized to asses profiles of airmass source when planning field campaigns. Questions on where, when or how long to measure in order to capture a certain mix of aerosol scenarios can easily be answered. In future the proposed method can be extended by further source maps, for example by dust source maps derived by the approach of Feuerstein and Schepanski (2018) or temporally varying information on wildfires as well as snow and ice cover or biological productivity.

Code and data availability. The processing software “trace_airmass_source” as used for this publication is available under Radenz (2020). The most recent version is available via GitHub: https://github.com/martin-rdz/trace_airmass_source (last access: 28.08.2020). A dockerfile is provied for a straightforward replication of the programming environment, including all dependencies. The data files are available on request.

https://doi.org/10.5194/acp-2020-955
Preprint. Discussion started: 12 October 2020

Author contributions. MR developed the algorithm and drafted the manuscript. PS, JB supported the implementation and supervised the work. HB, AF and YZ analyzed the lidar data. All authors jointly contributed to the manuscript and the scientific discussion.

Competing interests. The authors declare that they have no conflict of interest.

Acknowledgements. The research leading to these results has received funding from the European Union's Horizon 2020 research and innovation programme under grant agreement no. 654109 (ACTRIS), the European Union Seventh Framework Programme (FP7/2007–2013) under grant agreement no. 603445 (BACCHUS). We acknowledge funding from the Federal Ministry of Education and Research in Germany (BMBF) through the research program "High Definition Clouds and Precipitation for Climate Prediction – HD(CP)2" (grant nos. 01LK1503F,01LK1502I, 01LK1209C, and 01LK1212C). We thank the Alfred Wegener Institute and R/V Polarstern crew and captain for their support (AWI_PS113_00).

https://doi.org/10.5194/acp-2020-955
Preprint. Discussion started: 12 October 2020

References

ARL Archive: GDAS1 dataset, https://www.ready.noaa.gov/gdas1.php, 2019 (last accessed: 11.11.2019).

Ashbaugh, L. L.: A Statistical Trajectory Technique for Determining Air Pollution Source Regions, Journal of the Air Pollution Control Association, 33, 1096–1098, https://doi.org/10.1080/00022470.1983.10465702, 1983.

Ashbaugh, L. L., Malm, W. C., and Sadeh, W. Z.: A residence time probability analysis of sulfur concentrations at grand Canyon National Park, Atmospheric Environment (1967), 19, 1263 – 1270, https://doi.org/10.1016/0004-6981(85)90256-2, 1985.

Baars, H., Kanitz, T., Engelmann, R., Althausen, D., Heese, B., Komppula, M., Preißler, J., Tesche, M., Ansmann, A., Wandinger, U., Lim, J.-H., Ahn, J. Y., Stachlewska, I. S., Amiridis, V., Marinou, E., Seifert, P., Hofer, J., Skupin, A., Schneider, F., Bohlmann, S., Foth, A., Bley, S., Pfüller, A., Giannakaki, E., Lihavainen, H., Viisanen, Y., Hooda, R. K., Pereira, S. N., Bortoli, D., Wagner, F., Mattis, I., Janicka, L., Markowicz, K. M., Achtert, P., Artaxo, P., Pauliquevis, T., Souza, R. A. F., Sharma, V. P., van Zyl, P. G., Beukes, J. P., Sun, J., Rohwer, E. G., Deng, R., Mamouri, R.-E., and Zamorano, F.: An overview of the first decade of Polly$^{\mathrm{NET}}$: an emerging network of automated Raman-polarization lidars for continuous aerosol profiling, Atmospheric Chemistry and Physics, 16, 5111–5137, https://doi.org/10.5194/acp-16-5111-2016, 2016.

Baars, H., Seifert, P., Engelmann, R., and Wandinger, U.: Target categorization of aerosol and clouds by continuous multiwavelength-polarization lidar measurements, Atmospheric Measurement Techniques, 10, 3175–3201, https://doi.org/10.5194/amt-10-3175-2017, 2017.

Broxton, P. D., Zeng, X., Sulla-Menashe, D., and Troch, P. A.: A Global Land Cover Climatology Using MODIS Data, Journal of Applied Meteorology and Climatology, 53, 1593–1605, https://doi.org/10.1175/JAMC-D-13-0270.1, 2014.

Burton, S. P., Ferrare, R. A., Hostetler, C. A., Hair, J. W., Rogers, R. R., Obland, M. D., Butler, C. F., Cook, A. L., Harper, D. B., and Froyd, K. D.: Aerosol classification using airborne High Spectral Resolution Lidar measurements – methodology and examples, Atmospheric Measurement Techniques, 5, 73–98, https://doi.org/10.5194/amt-5-73-2012, 2012.

Dipu, S., Quaas, J., Wolke, R., Stoll, J., Mühlbauer, A., Sourdeval, O., Salzmann, M., Heinold, B., and Tegen, I.: Implementation of aerosol–cloud interactions in the regional atmosphere–aerosol model COSMO-MUSCAT(5.0) and evaluation using satellite data, Geoscientific Model Development, 10, 2231–2246, https://doi.org/10.5194/gmd-10-2231-2017, 2017.

Draxler, R. R.: Evaluation of an Ensemble Dispersion Calculation, Journal of Applied Meteorology, 42, 308–317, https://doi.org/10.1175/1520-0450(2003)042<0308:EOAEDC>2.0.CO;2, 2003.

Engelmann, R., Kanitz, T., Baars, H., Heese, B., Althausen, D., Skupin, A., Wandinger, U., Komppula, M., Stachlewska, I. S., Amiridis, V., Marinou, E., Mattis, I., Linné, H., and Ansmann, A.: The automated multiwavelength Raman polarization and water-vapor lidar Polly$^{\mathrm{XT}}$: the neXT generation, Atmospheric Measurement Techniques, 9, 1767–1784, https://doi.org/10.5194/amt-9-1767-2016, 2016.

Escudero, M., Stein, A., Draxler, R., Querol, X., Alastuey, A., Castillo, S., and Avila, A.: Source apportionment for African dust outbreaks over the Western Mediterranean using the HYSPLIT model, Atmospheric Research, 99, 518 – 527, https://doi.org/10.1016/j.atmosres.2010.12.002, 2011.

Feuerstein, S. and Schepanski, K.: Identification of Dust Sources in a Saharan Dust Hot-Spot and Their Implementation in a Dust-Emission Model, Remote Sensing, 11, 4, https://doi.org/10.3390/rs11010004, 2018.

Fleming, Z. L., Monks, P. S., and Manning, A. J.: Review: Untangling the influence of air-mass history in interpreting observed atmospheric composition, Atmospheric Research, 104-105, 1 – 39, https://doi.org/https://doi.org/10.1016/j.atmosres.2011.09.009, 2012.

https://doi.org/10.5194/acp-2020-955
Preprint. Discussion started: 12 October 2020

Atmospheric Chemistry and Physics Discussions

Flemming, J., Benedetti, A., Inness, A., Engelen, R. J., Jones, L., Huijnen, V., Remy, S., Parrington, M., Suttie, M., Bozzo, A., Peuch, V.-H., Akritidis, D., and Katragkou, E.: The CAMS interim Reanalysis of Carbon Monoxide, Ozone and Aerosol for 2003–2015, Atmospheric Chemistry and Physics, 17, 1945–1983, https://doi.org/10.5194/acp-17-1945-2017, 2017.

Floutsi, A. A., Baars, H., Radenz, M., Haarig, M., Yin, Z., Seifert, P., Jimenez, C., Wandinger, U., Engelmann, R., Barja, B., Zamorano, F., and Ansmann, A.: Biomass burning aerosols in the southern hemispheric midlatitudes as observed with a multiwavelength polarization Raman lidar, Atmospheric Chemistry and Physics Discussions, 2020, 1–27, https://doi.org/10.5194/acp-2020-453, https://www.atmos-chem-phys-discuss.net/acp-2020-453/, 2020.

Foth, A., Kanitz, T., Engelmann, R., Baars, H., Radenz, M., Seifert, P., Barja, B., Fromm, M., Kalesse, H., and Ansmann, A.: Vertical aerosol distribution in the southern hemispheric midlatitudes as observed with lidar in Punta Arenas, Chile (53.2° S and 70.9° W), during ALPACA, Atmospheric Chemistry and Physics, 19, 6217–6233, https://doi.org/10.5194/acp-19-6217-2019, 2019.

Friedl, M., McIver, D., Hodges, J., Zhang, X., Muchoney, D., Strahler, A., Woodcock, C., Gopal, S., Schneider, A., Cooper, A., Baccini, A., Gao, F., and Schaaf, C.: Global land cover mapping from MODIS: algorithms and early results, Remote Sensing of Environment, 83, 287–302, https://doi.org/https://doi.org/10.1016/S0034-4257(02)00078-0, 2002.

Groß, S., Esselborn, M., Weinzierl, B., Wirth, M., Fix, A., and Petzold, A.: Aerosol classification by airborne high spectral resolution lidar observations, Atmospheric Chemistry and Physics, 13, 2487–2505, https://doi.org/10.5194/acp-13-2487-2013, 2013.

Haarig, M., Ansmann, A., Gasteiger, J., Kandler, K., Althausen, D., Baars, H., Radenz, M., and Farrell, D. A.: Dry versus wet marine particle optical properties: RH dependence of depolarization ratio, backscatter, and extinction from multiwavelength lidar measurements during SALTRACE, Atmospheric Chemistry and Physics, pp. 14 199–14 217, https://doi.org/10.5194/acp-17-14199-2017, https://www.atmos-chem-phys.net/17/14199/2017/, 2017.

Hamilton, D. S., Lee, L. A., Pringle, K. J., Reddington, C. L., Spracklen, D. V., and Carslaw, K. S.: Occurrence of pristine aerosol environments on a polluted planet, Proceedings of the National Academy of Sciences, 111, 18 466–18 471, https://doi.org/10.1073/pnas.1415440111, 2014.

Heintzenberg, J., Birmili, W., Seifert, P., Panov, A., Chi, X., and Andreae, M. O.: Mapping the aerosol over Eurasia from the Zotino Tall Tower, Tellus B: Chemical and Physical Meteorology, 65, 20 062, https://doi.org/10.3402/tellusb.v65i0.20062, 2013.

Illingworth, A. J., Barker, H. W., Beljaars, A., Ceccaldi, M., Chepfer, H., Clerbaux, N., Cole, J., Delanoë, J., Domenech, C., Donovan, D. P., Fukuda, S., Hirakata, M., Hogan, R. J., Huenerbein, A., Kollias, P., Kubota, T., Nakajima, T., Nakajima, T. Y., Nishizawa, T., Ohno, Y., Okamoto, H., Oki, R., Sato, K., Satoh, M., Shephard, M. W., Velázquez-Blázquez, A., Wandinger, U., Wehr, T., and van Zadelhoff, G.-J.: The EarthCARE Satellite: The Next Step Forward in Global Measurements of Clouds, Aerosols, Precipitation, and Radiation, Bulletin of the American Meteorological Society, 96, 1311–1332, https://doi.org/10.1175/BAMS-D-12-00227.1, 2015.

Kahl, J. D.: A cautionary note on the use of air trajectories in interpreting atmospheric chemistry measurements, Atmospheric Environment. Part A. General Topics, 27, 3037 – 3038, https://doi.org/https://doi.org/10.1016/0960-1686(93)90336-W, arctic air, snow and ice chemistry, 1993.

Lu, Z., Streets, D. G., Zhang, Q., and Wang, S.: A novel back-trajectory analysis of the origin of black carbon transported to the Himalayas and Tibetan Plateau during 1996–2010, Geophysical Research Letters, 39, L01 809, https://doi.org/10.1029/2011GL049903, 2012.

Mamouri, R. E., Ansmann, A., Nisantzi, A., Kokkalis, P., Schwarz, A., and Hadjimitsis, D.: Low Arabian dust extinction-to-backscatter ratio, Geophysical Research Letters, 40, 4762–4766, https://doi.org/10.1002/grl.50898, 2013.

Matthias, V., Balis, D., Bösenberg, J., Eixmann, R., Iarlori, M., Komguem, L., Mattis, I., Papayannis, A., Pappalardo, G., Perrone, M. R., and Wang, X.: Vertical aerosol distribution over Europe: Statistical analysis of Raman lidar data from 10 European Aerosol Research Lidar

https://doi.org/10.5194/acp-2020-955
Preprint. Discussion started: 12 October 2020

Atmospheric Chemistry and Physics Discussions

Network (EARLINET) stations, Journal of Geophysical Research: Atmospheres, 109, D18 201, https://doi.org/10.1029/2004JD004638, 2004.

Mattis, I., Müller, D., Ansmann, A., Wandinger, U., Preißler, J., Seifert, P., and Tesche, M.: Ten years of multiwavelength Raman lidar observations of free-tropospheric aerosol layers over central Europe: Geometrical properties and annual cycle, Journal of Geophysical Research: Atmosphere, 113, https://doi.org/10.1029/2007JD009636, 2008.

Merrill, J. T., Bleck, R., and Avila, L.: Modeling atmospheric transport to the Marshall Islands, Journal of Geophysical Research: Atmospheres, 90, 12 927–12 936, https://doi.org/10.1029/JD090iD07p12927, 1985.

Müller, D., Ansmann, A., Mattis, I., Tesche, M., Wandinger, U., Althausen, D., and Pisani, G.: Aerosol-type-dependent lidar ratios observed with Raman lidar, Journal of Geophysical Research: Atmospheres, 112, https://doi.org/10.1029/2006JD008292, 2007.

Nisantzi, A., Mamouri, R. E., Ansmann, A., Schuster, G. L., and Hadjimitsis, D. G.: Middle East versus Saharan dust extinction-to-backscatter ratios, Atmospheric Chemistry and Physics, 15, 7071–7084, https://doi.org/10.5194/acp-15-7071-2015, 2015.

NOAA, N.: National Centers for Environmental Prediction FNL Operational Model Global Tropospheric Analyses continuing from July 1999, https://doi.org/https://doi.org/10.5065/D6M043C6, https://doi.org/10.5065/D6M043C6, 2000.

Paris, J.-D., Stohl, A., Ciais, P., Nédélec, P., Belan, B. D., Arshinov, M. Y., and Ramonet, M.: Source-receptor relationships for airborne measurements of CO_2, CO and O_3 above Siberia: a cluster-based approach, Atmospheric Chemistry and Physics, 10, 1671–1687, https://doi.org/10.5194/acp-10-1671-2010, 2010.

Pisso, I., Sollum, E., Grythe, H., Kristiansen, N. I., Cassiani, M., Eckhardt, S., Arnold, D., Morton, D., Thompson, R. L., Groot Zwaaftink, C. D., Evangeliou, N., Sodemann, H., Haimberger, L., Henne, S., Brunner, D., Burkhart, J. F., Fouilloux, A., Brioude, J., Philipp, A., Seibert, P., and Stohl, A.: The Lagrangian particle dispersion model FLEXPART version 10.4, Geoscientific Model Development, 12, 4955–4997, https://doi.org/10.5194/gmd-12-4955-2019, 2019.

Polissar, A., Hopke, P., Paatero, P., Kaufmann, Y., Hall, D., Bodhaine, B., Dutton, E., and Harris, J.: The aerosol at Barrow, Alaska: long-term trends and source locations, Atmospheric Environment, 33, 2441 – 2458, https://doi.org/https://doi.org/10.1016/S1352-2310(98)00423-3, 1999.

Radenz, M.: martin-rdz/trace_airmass_source: trace version of aug2020, https://doi.org/10.5281/zenodo.4008383, 2020.

Rieger, D., Bangert, M., Bischoff-Gauss, I., Förstner, J., Lundgren, K., Reinert, D., Schröter, J., Vogel, H., Zängl, G., Ruhnke, R., and Vogel, B.: ICON–ART 1.0 – a new online-coupled model system from the global to regional scale, Geoscientific Model Development, 8, 1659–1676, https://doi.org/10.5194/gmd-8-1659-2015, 2015.

Seibert, P.: Convergence and Accuracy of Numerical Methods for Trajectory Calculations, Journal of Applied Meteorology, 32, 558–566, https://doi.org/10.1175/1520-0450(1993)032<0558:CAAONM>2.0.CO;2, 1993.

Stein, A. F., Draxler, R. R., Rolph, G. D., Stunder, B. J. B., Cohen, M. D., and Ngan, F.: NOAA's HYSPLIT Atmospheric Transport and Dispersion Modeling System, Bulletin of the American Meteorological Society, 96, 2059–2077, https://doi.org/10.1175/BAMS-D-14-00110.1, 2015.

Stohl, A.: Trajectory statistics-A new method to establish source-receptor relationships of air pollutants and its application to the transport of particulate sulfate in Europe, Atmospheric Environment, 30, 579 – 587, https://doi.org/https://doi.org/10.1016/1352-2310(95)00314-2, 1996.

Stohl, A.: Computation, accuracy and applications of trajectories—A review and bibliography, Atmospheric Environment, 32, 947 – 966, https://doi.org/10.1016/S1352-2310(97)00457-3, 1998.

https://doi.org/10.5194/acp-2020-955
Preprint. Discussion started: 12 October 2020

Atmospheric Chemistry and Physics Discussions
Open Access
EGU

Stohl, A., Wotawa, G., Seibert, P., and Kromp-Kolb, H.: Interpolation Errors in Wind Fields as a Function of Spatial and Temporal Resolution and Their Impact on Different Types of Kinematic Trajectories, Journal of Applied Meteorology, 34, 2149–2165, https://doi.org/10.1175/1520-0450(1995)034<2149:IEIWFA>2.0.CO;2, 1995.

Stohl, A., Eckhardt, S., Forster, C., James, P., Spichtinger, N., and Seibert, P.: A replacement for simple back trajectory calculations in the interpretation of atmospheric trace substance measurements, Atmospheric Environment, 36, 4635 – 4648, https://doi.org/https://doi.org/10.1016/S1352-2310(02)00416-8, 2002.

Stohl, A., Forster, C., Frank, A., Seibert, P., and Wotawa, G.: Technical note: The Lagrangian particle dispersion model FLEXPART version 6.2, Atmospheric Chemistry and Physics, 5, 2461–2474, https://doi.org/10.5194/acp-5-2461-2005, 2005.

Strass, V. H.: The Expedition PS113 of the Research Vessel POLARSTERN to the Atlantic Ocean in 2018, https://doi.org/10.2312/BzPM_0724_2018, https://www.tib.eu/de/suchen/id/awi%3Adoi%7E10.2312%252FBzPM_0724_2018, 2018.

Tarasova, O. A., Senik, I. A., Sosonkin, M. G., Cui, J., Staehelin, J., and Prévôt, A. S. H.: Surface ozone at the Caucasian site Kislovodsk High Mountain Station and the Swiss Alpine site Jungfraujoch: data analysis and trends (1990–2006), Atmospheric Chemistry and Physics, 9, 4157–4175, https://doi.org/10.5194/acp-9-4157-2009, 2009.

Tesche, M., Ansmann, A., Müller, D., Althausen, D., Engelmann, R., Freudenthaler, V., and Groß, S.: Vertically resolved separation of dust and smoke over Cape Verde using multiwavelength Raman and polarization lidars during Saharan Mineral Dust Experiment 2008, Journal of Geophysical Research: Atmospheres, 114, D13 202, https://doi.org/10.1029/2009JD011862, 2009.

Tesche, M., Gross, S., Ansmann, A., Müller, D., Althausen, D., Freudenthaler, V., and Esselborn, M.: Profiling of Saharan dust and biomass-burning smoke with multiwavelength polarization Raman lidar at Cape Verde, Tellus B: Chemical and Physical Meteorology, 63, 649–676, https://doi.org/10.1111/j.1600-0889.2011.00548.x, 2011.

Val Martin, M., Kahn, R., and Tosca, M.: A Global Analysis of Wildfire Smoke Injection Heights Derived from Space-Based Multi-Angle Imaging, Remote Sensing, 10, 1609, https://doi.org/10.3390/rs10101609, 2018.

Veselovskii, I., Whiteman, D. N., Korenskiy, M., Suvorina, A., Kolgotin, A., Lyapustin, A., Wang, Y., Chin, M., Bian, H., Kucsera, T. L., Pérez-Ramírez, D., and Holben, B.: Characterization of forest fire smoke event near Washington, DC in summer 2013 with multi-wavelength lidar, Atmospheric Chemistry and Physics, 15, 1647–1660, https://doi.org/10.5194/acp-15-1647-2015, 2015.

Wernli, B. H. and Davies, H. C.: A lagrangian-based analysis of extratropical cyclones. I: The method and some applications, Quarterly Journal of the Royal Meteorological Society, 123, 467–489, https://doi.org/10.1002/qj.49712353811, 1997.

Winker, D. M., Tackett, J. L., Getzewich, B. J., Liu, Z., Vaughan, M. A., and Rogers, R. R.: The global 3-D distribution of tropospheric aerosols as characterized by CALIOP, Atmospheric Chemistry and Physics, 13, 3345–3361, https://doi.org/10.5194/acp-13-3345-2013, 2013.

Yin, Z. and Baars, H.: PollyNET/Pollynet_Processing_Chain: Version 2.0, https://doi.org/10.5281/zenodo.3774689, https://doi.org/10.5281/zenodo.3774689, 2020.

Yin, Z., Ansmann, A., Baars, H., Seifert, P., Engelmann, R., Radenz, M., Jimenez, C., Herzog, A., Ohneiser, K., Hanbuch, K., Blarel, L., Goloub, P., Dubois, G., Victori, S., and Maupin, F.: Aerosol measurements with a shipborne Sun–sky–lunar photometer and collocated multiwavelength Raman polarization lidar over the Atlantic Ocean, Atmospheric Measurement Techniques, 12, 5685–5698, https://doi.org/10.5194/amt-12-5685-2019, 2019.